JGR Solid Earth

RESEARCH ARTICLE
10.1029/2019JB017983

Equation of State for Shocked Fe-8.6 wt% Si up to 240 GPa and 4,670 K

Haijun Huang[1], Chunwei Leng[1], Qingsong Wang[2], Gang Young[1], Xun Liu[1], Ye Wu[1], Feng Xu[1], and Yingwei Fei[3]

[1]School of Sciences, Wuhan University of Technology, Wuhan, China, [2]National Key Laboratory of Shock Wave and Detonation Physics, Institute of Fluid Physics, China Academy of Engineering Physics, Mianyang, China, [3]Geophysical Laboratory, Carnegie Institution of Washington, Washington, DC, USA

Key Points:
- The equation of state of Fe-8.6 wt% Si alloy along Huogniot was measured up to 240 GPa using two-stage gas-gun technique
- The contents of Si in the outer core and the inner core are no more than 8.6 and 3.8 wt%, respectively
- The outer core may contain 5.6±3.0 wt% S and 3.8±2.9 wt% Si if both S and Si are considered as major elements in the core

Supporting Information:
- Supporting Information S1

Correspondence to:
H. Huang and Y. Fei,
hjhuang@whut.edu.cn;
yfei@carnegiescience.edu

Citation:
Huang, H., Leng, C., Wang, Q., Young, G., Liu, X., Wu, Y., et al. (2019). Equation of state for shocked Fe-8.6 wt% Si up to 240 GPa and 4,670 K. *Journal of Geophysical Research: Solid Earth*, *124*. https://doi.org/10.1029/2019JB017983

Received 8 MAY 2019
Accepted 9 AUG 2019
Accepted article online 16 AUG 2019

Abstract Using dynamic compression technique, the equation of state for Fe-8.6 wt% Si was measured up to 240 GPa and 4,670 K. A least squares fit to the experimental data yields the Hugoniot parameters C_0 = 4.603±0.101 km/s and λ = 1.505±0.037 with initial density ρ_0=7.386±0.021 g/cm^3. Based on the Hugoniot data, the calculated isothermal equation of state is consistent with static compression data when the lattice Grüneisen parameter γ_l =1.65(7.578/ρ) and electronic Grüneisen parameter γ_e=1.83. The calculated pressure-density data at 300 K were fitted to a third-order Birch-Murnaghan equation of state with zero pressure the parameters K_0=192.1±6.3 GPa, $K_0^{'}$=4.71±0.27 with fixed $\rho_{0\varepsilon}$ =7.578±0.050 g/cm^3. Under the conditions of Earth's core, the densities of Fe-8.6±2.0 wt% Si and Fe-3.8±2.9 wt% Si agree with preliminary reference Earth mode (PREM) data of the outer and the inner core, respectively. These are the upper limits for Si in the core assuming Si is the only light element. Simultaneously considering the geophysical and geochemical constraints for a Si-S-bearing core, the outer core may contain 3.8±2.9 wt% Si and 5.6±3.0 wt% S.

Plain Language Summary Silicon (Si) may be a dominant light element in the core, and precise evaluation of its amount requires accurate thermal equation of state of Fe-Si alloy. Here we present the Hugoniot data for Fe-8.6 wt% Si, measured up to 240 GPa with two-stage light gas gun. The experimental data allow us to establish reliable thermal equation of state of Fe-Si alloy over a wide pressure-temperature range and to constrain the composition of the core. The results indicate that the densities of Fe-8.6 wt% Si and Fe-3.8 wt% Si agree with the observed density profiles of the outer core and the inner core, respectively. Our model prefers an Fe-Si-S core that contains about 3.8±2.9 wt% Si and 5.6±3.0 wt% S in the outer core.

1. Introduction

Based on cosmochemical constraints, high-pressure experiments, and seismic data, the Earth's outer core consists of mainly iron and small amounts of light elements, such as O (oxygen), S (sulfur), Si (silicon), C (carbon), and H (hydrogen; Birch, 1952; Hillgren et al., 2000; Hirose et al., 2013; Li & Fei, 2003; Mao et al., 1990; Poirier, 1994). Among these light elements, Si has been proposed as one of the major candidates for the following reasons. First of all, it is one of the most abundant elements in the Earth (Birch, 1964; Ringwood, 1959). Second, the high solubility of silicon in iron at high pressures and temperatures supports its existence in Earth's core (Fischer et al., 2012, 2013, 2014; Ozawa et al., 2016; Sakai et al., 2006; Takafuji et al., 2005; Tateno et al., 2015). Third, relative to C1 chondritic material, the depletion of Si in Earth's mantle indicates that Si might be incorporated into the core (Allègre et al., 1995; Ringwood, 1959; Wänke & Gold, 1981). Fourth, the chemical reaction of liquid iron with silicate producing a silicon-iron alloy provides a plausible mechanism for Si entering to the core (Dubrovinsky et al., 2003; Knittle & Jeanloz, 1991).

In order to estimate the Si content in the core, many research groups have been focused on the equation of state (EOS) of Fe-Si alloys, but no consensus has been reached so far (Asanuma et al., 2011; Balchan & Cowan, 1966; Fischer et al., 2012, 2014; Hirao et al., 2004; Lin et al., 2003; Tateno et al., 2015; Zhang et al., 2016, 2018). For example, using shock compression method, Balchan and Cowan (1966) investigated the EOS of Fe-4 wt% Si and Fe-19.8 wt% Si, and they suggested that Earth's outer core contains about 14–20 wt% Si. According to the EOS and sound velocity of Fe-9Ni-10Si along Hugoniot measured by Zhang et al. (2016), the content of Si in the outer core is no more than 10 wt%. Using static compression technique at 300 K, Lin et al. (2003) measured the EOS for Fe-Si system, and they concluded about 8–10 wt% Si in

the outer core and 4 wt% Si in the inner core. Experimental data and ab initial calculations by Fischer et al. (2014) indicate that the maximum amount of Si in the outer core and the inner core is 11 and 6–8 wt%, respectively. Most recently, static compression data by Tateno et al. (2015) support that the inner core contains about 7 wt% Si.

Here we use dynamic compression technique to obtain new pressure-density relation for well-characterized Fe-9Si alloy up to 240 GPa along Hugoniot. Using the new data, we derive the thermodynamic parameters of Fe-9Si and evaluate consistency of the existing static compression data. Finally, we estimate the content of Si in the outer core and the inner core based on our thermodynamic model.

2. Materials and Methods

2.1. Sample Preparation

The starting material is iron-silicon alloy, Fe-9Si powder, from Goodfellow Co. Ltd. The average grain size of the powder is about 10 μm. The content of Si in the alloy powder ranges from 8.7±0.3 wt% (Hirao et al., 2004) to 8.75±0.40 wt% (Fischer et al., 2013) and 8.87±0.54 wt% (Zhang & Guyot, 1999). Under ambient condition, although the Fe-9Si powder was from Goodfellow Co. Ltd, their structure is controversial. For example, according to the X-ray diffraction patterns, Zhang and Guyot (1999) and Hirao et al. (2004) proposed that powdered Fe-9Si has a body-centered cubic (bcc) structure (space group Im3m). Fischer et al. (2014, 2013) suggested that Fe-9Si alloy has $D0_3$ structure (BiF_3-type; space group Fm3m) because they found three to seven hkl peaks in their diffraction patterns. Our measured X-ray diffraction pattern (D8 Advance) has three hkl peaks, which indicated that the structure of powder Fe-9Si is bcc (Figure 1a). The lattice parameter and unit-cell volume are a_0=2.845 (1) Å and V_0=23.03 (3) Å^3, which are consistent with a_0= 2.8429(8) Å and V_0= 22.976(20) Å^3 (Zhang & Guyot, 1999) and a_0= 2.8437(3) Å and V_0= 22.995(6) Å^3 (Hirao et al., 2004).

For our shock wave experiments, we need a dense, bulk sample. Using a multianvil high-pressure device in Wuhan University of Technology, we sintered the Fe-9Si alloy powder at pressure ~4 GPa and temperature ~1,200 °C. The bulk samples were polished to a flat disc with a tolerance of~0.002 mm. The diameter of the disc was about 12 mm, and the thickness varied from 1.77 to 2 mm. The X-ray diffraction pattern (Figure 1a) showed that the structure of Fe-9Si alloy is still bcc after sintering. The electron microprobe (JEOL-JXA8530F) analyses (Table S1 in the supporting information) showed Si is uniformly distributed in the sample with an average content of 8.62±0.03 wt% Si ($Fe_{0.84}Si_{0.16}$ by mole, hereafter Fe-9Si). According to the backscattered electron image (JSM-7500F), the grain size in the sintered sample is no more than ~20 μm, and no detectable porosity in the sintered sample (Figure 1b). Because the distribution of Si in the sample is uniform according to Table S1, the contrast in Figure 1b cannot be caused by the composition. And it might be caused by the different orientation of each grain. From energy-dispersive X-ray images (Figures 1c and 1d), Fe and Si are homogenously distributed in the bulk sample. According to the unit-cell volume obtained from X-ray diffraction patterns, the density of the powder sample is ρ_0= 7.419±0.011 g/cm^3, which is very close to the average bulk density 7.386 ±0.021 g/cm^3 measured by the Archimedean method. Therefore, the porosity of the bulk sample is less than 0.5%.

2.2. Experimental Methods

The EOS of Fe-9Si under shock compression is determined by Rankine-Hugoniot relation (Mitchell & Nellis, 1981)

$$P_H - P_0 = \rho_0 (D_S - u_0)(u - u_0), \tag{1}$$

$$V_H = V_0[1 - (u - u_0)/(D_S - u_0)], \tag{2}$$

$$E_H - E_0 = \frac{1}{2}(P_H + P_0)(V_0 - V). \tag{3}$$

The symbol P represents the pressure. ρ and V are density and specific volume. E is the specific internal energy. D_S represents the velocity of the shock wave. The particle velocity of the sample is expressed as u. Subscripts H and 0 indicate the Hugoniot state and initial state. D_S and u for Fe-9Si were measured using two-stage light gas gun at the Institute of Fluid Physics of China Academy of Engineering Physics and at

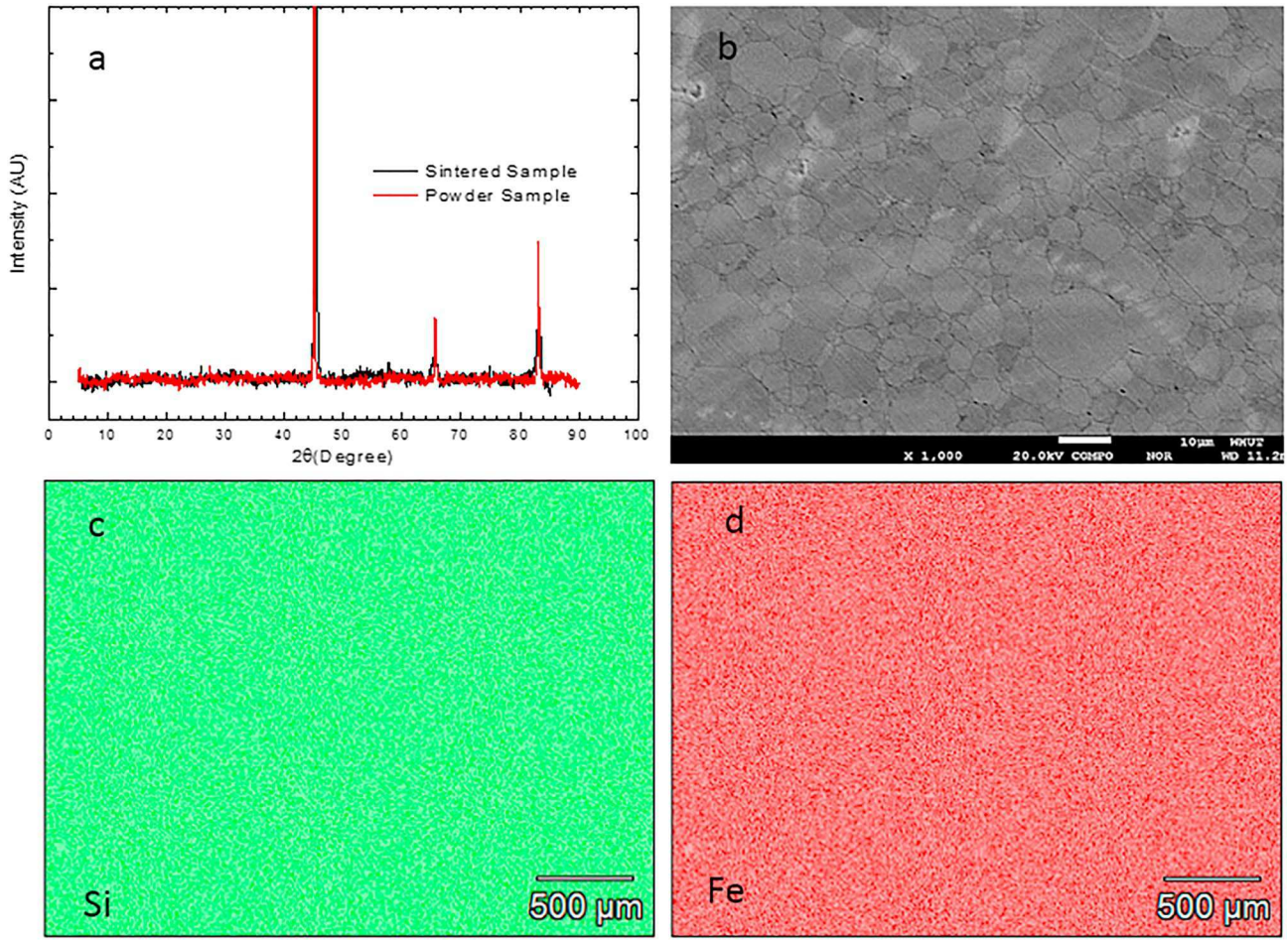

Figure 1. (a) X-ray diffraction patterns of powder sample and sintered sample. (b) Backscattered electron image of the Fe-9 Si alloy. (c) Distribution of Si in the sample measured using energy dispersive X-ray spectroscopy. (d) Distribution of Fe in the sample measured using energy dispersive X-ray spectroscopy.

the High Pressure Physics and Novel Materials Research Center in Wuhan University of Technology using the reverse-impact and impedance-matching techniques described below.

2.2.1. Reverse-Impact Technique

The reverse-impact technique has been described by Duffy and Ahrens (1995). The diagram of the target was shown in Figure S1 (Huang et al., 2011, 2018). For this technique, a single crystal lithium fluoride (LiF) was used as window. In order to avoid the effect of the high pressure gas in the launching tube on the signal and to get a good reflective surface, in front of the LiF, we coated an aluminum film and mounted an aluminum foil with epoxy. The thicknesses of the aluminum film and foil are about 3 and 8 μm, respectively. A displacement interferometer system for any reflector (Weng et al., 2006) was used to measure the particle velocity u of the Al/LiF interface. When the flyer made of Fe-9Si impacted the LiF window with the velocity W, the shock waves were generated in the flyer and window, and the particle velocity u of the window increases immediately and remains constant. Figure S2 shows the experimental signals measured by displacement interferometer system for any reflector. In equation (1), the initial particle velocity u_0 for the Fe-9Si flyer and LiF window are W and zero, respectively. According to boundary and continuity conditions, the particle velocities u and pressure P_H of the flyer and LiF window should be equal.

$$P_H = \rho_{0,f}\left(-D_{S,f}-W\right)(u-W) = \rho_{0,W}\left(C_{0,W}+\lambda_W u\right)u \tag{4}$$

Substituting the Hugoniot parameters for LiF $C_{0,w}$=5.148 km/s, λ_w=1.353, and $\rho_{0,w}$=2.638g/cm^3 (Marsh, 1980) into equation (4), we solved the shock wave velocity and pressure in the flyer (Table 1).

Table 1
The Experimental Data for Fe-9Si

Shot no.	Initial density (g/cm^3)	Flyer	Impact velocity (km/s)	Shock velocity (km/s)	Particle velocity (km/s)	Pressure (GPa)	Compressed density (g/cm^3)	Shock temperature (K)
20150324[a]	7.364	Sample	2.021 (7)	5.55 (8)	0.631 (8)	25.8 (0.8)	8.31 (3)	407 (17)
20150326[a]	7.385	Sample	3.792 (7)	6.29 (8)	1.244 (8)	57.8 (0.9)	9.21 (4)	790 (44)
20160823[a]	7.362	Sample	3.830 (5)	6.46 (9)	1.242 (11)	59.1 (1.1)	9.11 (4)	730 (40)
20150325[a]	7.357	Sample	4.960 (7)	7.06 (7)	1.632 (8)	84.7 (1.0)	9.57 (3)	1,099 (78)
20150608[a]	7.385	Sample	6.139 (6)	7.67 (7)	2.040 (9)	115.6 (1.3)	10.06 (4)	1,709 (142)
20150609[a]	7.378	Sample	6.940 (7)	8.10 (7)	2.322 (11)	138.8 (1.4)	10.34 (4)	2,186 (192)
20150610[a]	7.391	Sample	7.692 (6)	8.43 (6)	2.597 (11)	161.9 (1.5)	10.68 (4)	2,896 (270)
20150331[b]	7.385	cu	3.903 (6)	7.80 (9)	2.001 (18)	115.3 (1.7)	9.94 (5)	1,534 (127)
20150401[b]	7.418	cu	4.682 (7)	8.25 (8)	2.420 (19)	148.0 (1.9)	10.50 (6)	2,497 (224)
20150330[b]	7.378	cu	5.602 (7)	8.97 (13)	2.905 (23)	192.2 (3.2)	10.91 (9)	3,482 (344)
20150327[b]	7.386	cu	6.485 (6)	9.68 (13)	3.360 (25)	240.3 (3.7)	11.31 (9)	4,670 (477)

[a]Reveres-impact experiments. The data in parentheses are uncertainties. Shock temperatures T_H are not directly measured but were calculated using the thermodynamic parameters determined in this study. [b]Impedance-matching experiments.

2.2.2. Impedance-Matching Technique

In the work reported by Huang et al. (2013), the impedance-matching technique was described. The diagram of the target was shown in Figure S3a. When the flyer impacted the base plate with velocity W, two shock waves were generated in the flyer and baseplate. According to boundary and continuity conditions, the pressure and particle velocity in the flyer and base plate are equal, P_f=P_b, u_f=u_b.

$$P_H = \rho_{0,f}\left[-C_{0,f} + \lambda_f\left(u_f - W\right)\right]\left(u_f - W\right) = \rho_{0,b}\left(C_{0,b} + \lambda_b u_b\right)u_b \tag{5}$$

Subscripts f and b represent the flyer and base-plate, which were both made of copper with Hugoniot parameters $C_{0,b}$=3.933 km/s, λ_b=1.500 (Mitchell & Nellis, 1981). Substituting the measured W and Hugoniot parameters in equation ((5)), we can obtain the particle velocity u_b and velocity of shock wave Ds in the base plate. As Ds reached the interface between base plate and the sample, a rarefaction wave propagated backward in the base plate, and a shock wave propagated forward in the sample if the impedance of the base plate is higher than that of sample (Jing, 1986). The velocity of D_S in the sample was measured by electrical pins placed on the base plate and sample. The distributions of the electrical pins were shown in Figure S3b. The tilt and distortion of the flyer were determined according to the method given by Mitchell and Nellis (1981).

$$\Delta t = t_{ji} - t_j = \frac{-R_j \tan\theta}{W}\cos(\alpha_0 + \alpha_i) \tag{6}$$

Subscript i means the ith electrical pin, and j means the jth circle (j = 1, 2, 3). α_i is the angular position of the ith electrical pin. R_j is the radius of the jth circle, and R_1=9mm, R_2=7mm, and R_3=4mm. t_j means the average time on the jth circle. For example, for the experiment 20150330†, the fitted tilt angles θ are 0.73° and 0.7° for Circles 2 and 3, respectively (Figure S3b). This implies that the shock wave propagated through the sample with nearly constant tilt angle. Usually, the distortion is modeled as an axially symmetric parabolic bow t'_j=aR^2_j+b, where the parameter b for the experiment 20150330† equals to the time t_0=210.22 ns measured by the center electrical pin, and a=(t_3-t_0)/R^2_3=0.2425 ns/mm^2. Thus, the transit time equals Δt=t'_2-t_2=t_3-t_2-Δt_c. For the experiment 20150330†, the correction time Δt_c caused by the distortion is about 4.8%. Then we obtained the shock velocity D_S=d/Δt, where d is the thickness of the sample. The pressure P_H and particle velocity u in the sample were calculated by the following equation.

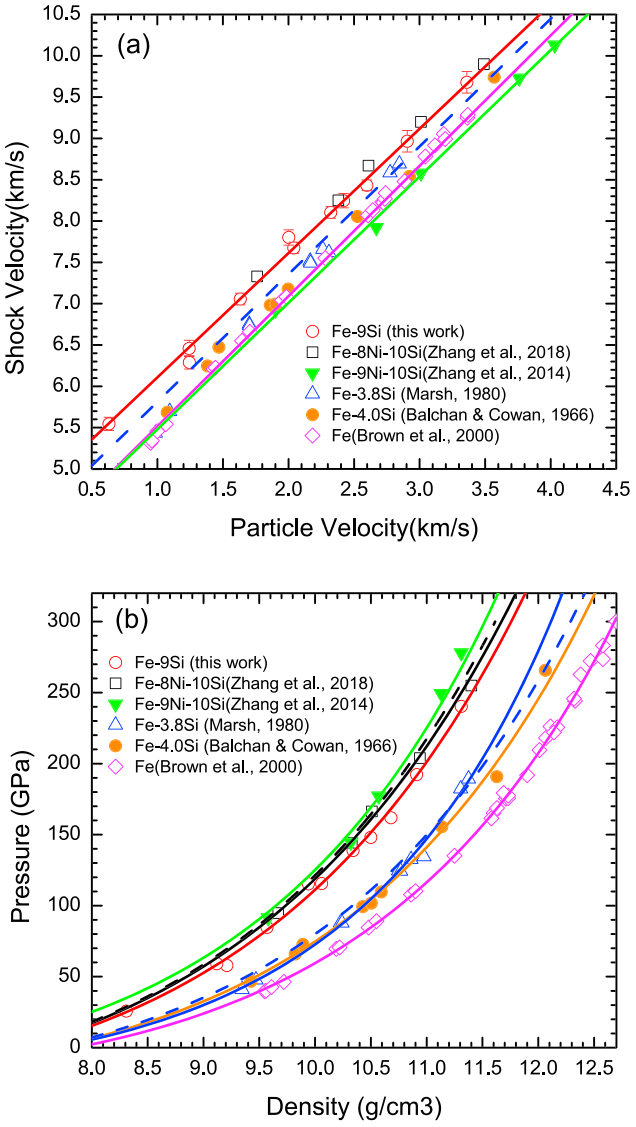

Figure 2. Hugoniot data for Fe-Si system. (a) Shock velocities D_S versus particle velocity u for Fe-Si system. (b) Pressure increases with density along Hugoniot for Fe-Si system. Open circles represent Fe-9Si (this work). Green down triangles and open squares represent Fe-9Ni-10Si (Zhang et al., 2014) and Fe-8Ni-10Si (Zhang et al., 2018). Solid circles, open triangles, and open diamonds represent Fe-4Si (Balchan & Cowan, 1966), Fe-3.8Si (Marsh, 1980), and pure Fe (Brown et al., 2000). Solid lines are the fitted results of experimental data. Dashed lines are the calculated results for Fe-3.8Si and Fe-10Si based on the additive law.

$$P_H = \rho_{0b}[-C_{0b} + \lambda_b(u-2u_b)](u-2u_b) = \rho_{0s}uD_s \quad (7)$$

3. Results and Geophysical Implication

3.1. EOS Along Hugoniot for Fe-Si

Table 1 lists the experimental data for the Fe-9Si alloy from 25.8 to 240.3 GPa. Figure 2 plots the D_S-u and P_H-ρ data. The shock velocities D_S and particle velocities u were fitted by a linear equation,

$$D_S = C_0 + \lambda u. \quad (8)$$

The fitted Hugoniot parameters are C_0=4.551±0.077 km/s and λ=1.526±0.035. We also fixed the initial density ρ_0=7.386 g/cm^3 and fitted the pressure P_H and density ρ using the following equation:

$$P_H = \rho_0 C_0^2(1-\rho_0/\rho)/[1-\lambda(1-\rho_0/\rho)]^2. \quad (9)$$

The fitted Hugoniot parameters are C_0=4.603±0.101 km/s and λ=1.505±0.037. The fitted result is slightly different from that of the D_S-u relationship, but it is considered more reliable because the initial density used in equation (9) is normalized. In Figure 2b, we also plotted the P_H-ρ data for iron (Brown et al., 2000), Fe-3.8Si (by weight, Marsh, 1980), Fe-4.0Si (by weight, Balchan & Cowan, 1966), Fe-9Ni-10Si (by weight, Zhang et al., 2014), and Fe-8Ni-10Si (by weight, Zhang et al., 2018) for comparison. The data of Fe-9Si are close to the data of Fe-8Ni-10Si (Zhang et al., 2018) but differ from their earlier data on Fe-9Ni-10Si (Zhang et al., 2014). The difference may be caused by the presence of SiO_2, and Si-rich silicides (Fe_3Si_7 and $FeSi_2$) in their sample. The Hugoniot data of Fe-3.8Si (Marsh, 1980) and Fe-4Si (Balchan & Cowan, 1966) fall between the results of pure iron (Brown et al., 2000) and our Fe-9Si data. Based on the Hugoniot data for iron (Brown et al., 2000) and Fe-9Si, we calculated the EOS of Fe-3.8Si and Fe-10Si along Hugoniot shown as the dashed lines in Figure 2b according to the additive law (Al'tshuler & Sharipdzhanov, 1971).

$$V(P) = \sum_i m_i V_{0i}\left\{1-\frac{1}{2\lambda_i^2}\left(\left(2\lambda_i+\frac{C_{0i}^2}{V_{0i}P}\right)-\sqrt{\left(2\lambda_i+\frac{C_{0i}^2}{V_{0i}P}\right)^2-4\lambda_i^2}\right)\right\} \quad (10)$$

Subscript i represents the component i and m is the weight percent of the component. V_0 is the specific volume at ambient conditions, and C_0 and λ are the Hugoniot parameters. The calculated results are in general agreement with those of Fe-3.8Si (Marsh, 1980) and Fe-4.0Si (Balchan & Cowan, 1966), and Fe-8Ni-10Si (Zhang et al., 2018), but there is a slightly systematic offset (~2%) below 189 GPa (Figure 2b). At same pressure, the density of Fe-8Ni-10Si is about 1.3 wt% lower than that of Fe-8.6Si due to the content of Si in the sample. The comparison demonstrates that the effect of Si on the EOS is systematic and can be reliably modeled using the additive law. All the Hugoniot parameters for Fe-Si system are summarized in Table 2.

3.2. The Isothermal EOS and Shock Temperatures for Fe-Si

From the Hugoniot data $P_H(V)$, we can calculate the isothermal pressure as a function of specific volume, $P_T(V)$, for Fe-9Si at a given temperature T according to Mie-Grüneisen EOS:

Table 2
The Hugoniot Parameters for Fe, Fe-Si, and Fe-Ni-Si Alloys

Alloy	Density (g/cm^3)	C_0 (km/s)	λ	Reference
Fe-9Ni-10Si	6.853 (36)	3.95 (15)	1.53 (5)	Zhang et al. (2014)
Fe-8Ni-10Si	7.352 (5)	4.75 (9)	1.48 (3)	Zhang et al. (2018)
Fe-3.8Si	7.652	3.785 (10)	1.716 (4)	Marsh (1980)
Fe-4Si	7.646	4.072 (123)	1.563 (57)	Balchan and Cowan (1966)
Fe	7.85	3.935 (29)	1.578 (10)	Brown et al. (2000)
Fe-9Si	7.386 (21)	4.603 (101)	1.505 (37)	This work
Fe-3.8Si	7.638	4.226 (121)	1.546 (60)	This work[a]

[a]Calculated based on the Hugoniot data of Fe and Fe-9Si.

$$P_T(V) = P_H(V) - \frac{1}{V}\int_T^{T_H} C_V \gamma_{eff} dT. \quad (11)$$

T_H is the shock temperatures, which can be estimated via the following thermodynamic relations (Brown & McQueen, 1986).

$$dT = -T\frac{\gamma_{eff}}{V}dV + \frac{1}{2C_V}\left[P_H(V) + (V_0 - V)\frac{dP_H(V)}{dV}\right]dV, \quad (12)$$

$$C_V = C_{Vl} + C_{Ve}, \quad (13)$$

$$\gamma_{eff} = (\gamma_l C_{Vl} + \gamma_e C_{Ve})/C_V. \quad (14)$$

C_{Vl} is the specific heat contributed by the lattice. At high temperature $C_{Vl}=3R/\mu$, where R is the gas constant and μ is the molar mass for Fe-9Si. At high pressure and temperature, Fe-9Si is in hcp (hexagonal close-packed) or hcp+B2 (CsCl-type) phase (Fischer et al., 2014), so we assumed its electronic specific heat is similar to that of hcp iron $C_{Ve}=\beta_0(\rho_{0\varepsilon}/\rho)^{\kappa}T$, where $\beta_0=0.091$ J·mg^{-1}·K^{-2} and $\kappa = 1.34$ (Boness et al., 1986). Here $\rho_{0\varepsilon}$ should be the density of Fe-9Si in hcp structure at 1 Bar and 300 K, rather than the initial density in bcc phase $\rho_{0\alpha}$ = 7.386 ±0.021 g/cm^3 measured by the Archimedean method. In equation (14), the effective Grüneisen parameter γ_{eff} should also include the lattice contribution $\gamma_l=\gamma_0(\rho_{0\varepsilon}/\rho)^q$ and electronic contribution γ_e (Anderson, 2002). Fischer et al. (2014) proposed that the lattice, anharmonic, or electronic contributions to thermal pressure variation can be described by γ_0 and q. Based on the P-V data measured at high pressure and temperature for hexagonal close-packed (hcp) structure and hcp+B2 (CsCl-type) structure, Fischer et al. (2014) suggested $\gamma_0=1.14\pm0.14$, $q=1$ (hcp Fe-9Si) and $\gamma_0=2.22\pm0.08$, $q=1$ (hcp+B2 Fe-9Si). According to the measured shock temperature of Fe-8Ni-10Si, Zhang et al. (2018) proposed $\gamma_0=2.7\pm0.2$, $q=0.4\pm0.1$. If we substitute these Grüneisen parameters into equations (11) and (12) without considering the contributions of electrons, the calculated isothermal EOS at 300 K does not match the experimental data (Tateno et al., 2015) (Figure 3). Therefore, it seems that the Grüneisen parameters for hcp Fe-9Si suggested by Fischer et al. (2014) and Zhang et al. (2018) are not consistent with the static and dynamic data. Here we only compared with the data measured by Tateno et al. (2015). So far, the EOS for hcp Fe-9Si has been measured by Hirao et al. (2004), Fischer et al. (2014), and Tateno et al. (2015), respectively. All the parameters were list in Table 3. Hirao et al. (2004) did not use pressure medium; thus, the nonhydrostatic condition affects the accuracy of the EOS. At high pressure and temperature, Fischer et al. (2014) measured the EOS for Fe-9Si and calculated the EOS at 300 K based on the $\gamma_0=1.14\pm0.14$, $q=1$. Tateno et al. (2015) directly measured the EOS of Fe-9Si up to 304.9 GPa at 300 K and high temperature. Fitting the data measured by Tateno et al. (2015) to third-order Birch-Murnaghan EOS yields $\rho_{0\varepsilon}$ =7.578 ±0.050 g/cm^3, K_0=190.0±11.3 GPa, and K_0'=4.76±0.14. Hereafter, we adopted $\rho_{0\varepsilon}$ =7.578 ±0.050 g/cm^3 to establish the EOS of Fe-9Si.

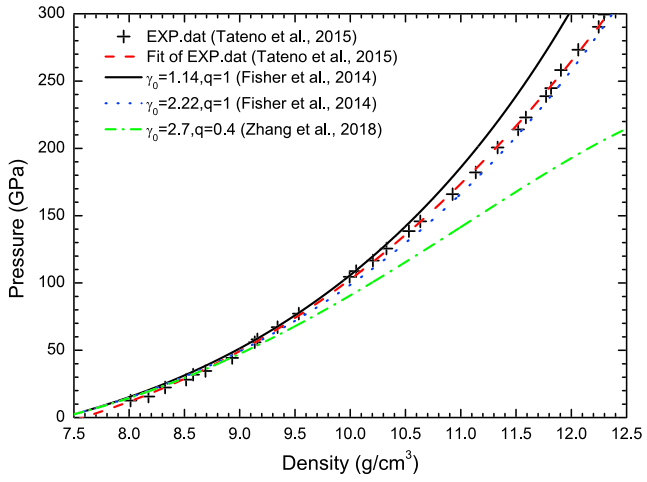

Figure 3. The calculated equation of state for Fe-9Si at 300 K according to the Hugoniot data and Grüneisen parameters. The crosses and red dash line represent the experimental data and fitted results at 300 K (Tateno et al., 2015). Black solid line represent the calculated results when $\gamma_0=1.14$ and $q=1$ for hcp Fe-9Si (Fischer et al., 2014). Blue dot line was the calculated result when $\gamma_0=2.22$ and $q=1$ for hcp+B2 Fe-9Si (Fischer et al., 2014). Assuming the Grüneisen parameter of Fe-9Si close to $\gamma_0=2.7$ and $q=0.4$ of Fe-8Ni-10Si (Zhang et al., 2018), the estimated equation of state was shown as the green dot-dash line.

It is important to consider the contributions of both lattice and electrons to the Grüneisen parameter for the model, especially at simultaneous high pressure and temperature. In order to evaluate the lattice and electron contribution, we tested various values of γ_0, q, and γ_e. The calculated EOS at 300, 1,200, 2,000, 3,000, 4,000, and 5,200 K were compared with the experimental data (Fischer et al., 2014; Tateno et al., 2015). When using $\gamma_0=1.65$, $q=1$, and $\gamma_e=1.83$, the calculated isothermal EOS are in good agreement with experimental data (Figure 4). Up to 400 GPa and 5,200 K, the differences of pressure between our calculated

Table 3
The Parameters of Birch-Murnaghan Equation of State for Fe-Si Alloy at 300 K

Alloy and structure	ρ_0 (g/cm^3)	K_0 (GPa)	K'_0	Reference
Fe-9Si (hcp)	7.67 (20)	198 (9)	4.7 (3)	Hirao et al. (2004)
Fe-9Si (hcp)	7.145 (53)	129.1 (1.4)	5.20 (8)	Fischer et al. (2014)
Fe-9Si (hcp+B2)	7.452 (18)	170.8 (1.6)	4.49 (7)	Fischer et al. (2014)
Fe-9Si (hcp)	7.578 (50)	190.0 (11.3)	4.76 (14)	Tateno et al. (2015)[a]
Fe-9Si (hcp)	7.578 (50)	190.8 (6.7)	4.74 (28)	This work[b]
Fe-9.8Ni-4Si (hcp)	7.975	174 (8)	4.79 (5)	Asanuma et al. (2011)
Fe-3.8Si (hcp)	7.949 (50)	181.9 (11.0)	4.67 (35)	This work[b]
Fe (hcp)	8.269[a]	172.7 (1.4)	4.79 (5)	Fei et al. (2016)

[a]Tateno et al. (2015) fitted the experimental data to the Vinet equation of state, and we refitted their data to third-order Birch-Murnaghan equation of state. [b]The data were estimated according to the Hugoniot data and Grüneisen equation of state.

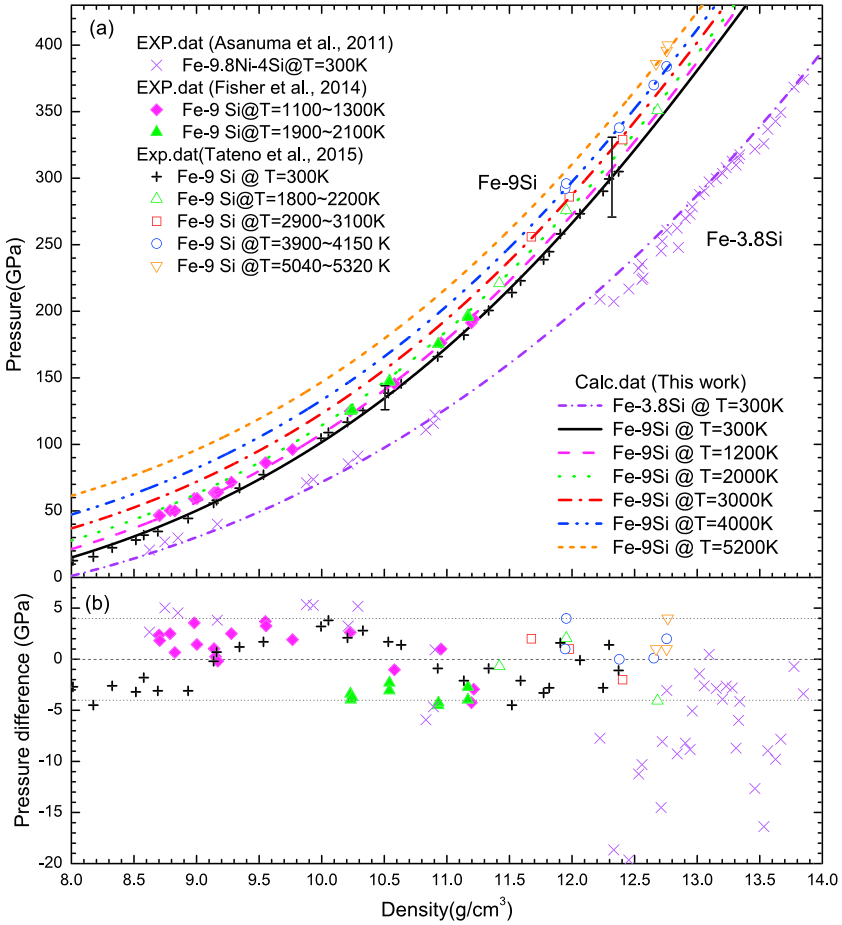

Figure 4. (a) The pressure versus density of Fe-Si system along different isotherm. All the lines represent the calculated pressure based on our Hugoniot data and Grüneisen equation of state. Symbols represent the static experimental data measured at different pressure and temperature. The data measured by Fischer et al. (2014) are shown as solid diamonds (1,100–1,300 K), solid triangles (1,900~2,100 K). The data measured by Tateno et al. (2015) are shown as plus (300 K), open triangle (1,800–2,200 K), open square (2,900–3,100 K), open circle (3,900–4,150 K), and open down triangle (5,040–5,320 K), respectively. Crosses represent the data of Fe-9.8Ni-4Si (Asanuma et al., 2011). The errors of pressure mainly caused by Hugoniot parameters are 6% and 10% at the pressure 135 and 300 GPa. (b) The difference of measured pressure and calculated results for Fe-9Si at same density and temperature. Up to 5,000 K and 400 GPa, the pressure differences for Fe-9Si range between 4 and −4 GPa. At 300 K, the pressure differences between Fe-3.8Si and Fe-9.8Ni-4Si vary from −6 to 5 GPa below 210 GPa and vary from −20 to 0 GPa up to 370 GPa.

Table 4
The Thermodynamic Parameters for hcp Fe-Si Alloys

Iron compound	β_0 J·kg^{-1}·K^{-2}	κ	γ_0	q	γ_e
Fe	0.091[a]	1.34[a]	1.74[b]	0.78[b]	2.0[c]
Fe-9Si	0.091[a]	1.34[a]	1.65[d]	1[d]	1.83[d]
Fe-3.8Si	0.091[a]	1.34[a]	1.74[c]	0.78[c]	2.0[c]

[a]Boness et al. (1986). [b]Fei et al. (2016). [c]Anderson (2002). [d]This work.

results and experimental data for Fe-9Si range between −4 and 4 GPa, which are within the experimental uncertainty (Figure 4). Fitting our calculated isothermal EOS at 300 K to third-order Birch-Murnaghan EOS, fixing $\rho_{0\varepsilon}$ =7.578 ±0.050 g/cm^3, we obtain K_0=190.8±6.7 GPa and K_0'=4.74±0.28. The uncertainties are mainly caused by the uncertainties in the fitted Hugoniot parameters. The agreements between our calculated results and experimental data showed that specific heat and Grüneisen parameter (Table 4) used in this work are self-consistent.

According to equations (11) and (12), the isothermal EOS and shock temperature were simultaneously calculated. Figure 5 shows the calculated shock temperatures compared with existing phase stability data of Fe-9Si at high pressure and temperature (Fischer et al., 2013; Hirao et al., 2004; Lin et al., 2003; Tateno et al., 2015). We infer that the shocked Fe-9Si has bcc structure at low pressure and converts to hcp structure at moderate pressure and temperature up to 145(±4) GPa and 2,400(±190) K. Above 145(±4) GPa and 2,400(±190) K, the static compression experiments revealed that hcp Fe-9Si only partially transforms to B2 (CsCl-type) structure because of the kinetic hindrance of the transition (Fischer et al., 2014; Tateno et al., 2015). From the Hugoniot data we found no detectable kink in the shock velocities and density, implying that either only a small quantity or no Fe-9Si might change to B2 structure during shock compression. Because the compression time of shock wave is much shorter than that of static compression technique, a sluggish phase transition is often not detectable. At ultrahigh pressure (>250 GPa), the Fe-9Si is expected to be melt and shocked into liquid state. Due to lack of experimental data on sound velocity of Fe-9Si, its onset melting along Hugoniot cannot be determined in this work. So we simply estimated according to intersection of the shock temperature for Fe-9Si and the melting curve of Fe-8Ni-10Si (Zhang et al., 2018). The melting temperatures of Fe-8Ni-10Si obtained using dynamic compression technique are lower than the extrapolated data of Fe-9Si (Fischer et al., 2013) according to Simon equation (Simon & Glatzel, 1929). This difference may not be caused by the addition of Ni because the melting temperature of Fe-5Ni-10Si (Morard et al., 2011) is consistent with Fe-9Si (Fischer et al., 2013) up to 50 GPa. Therefore, the difference of the melting temperature could be caused by the different phase of Fe-9Si. The phase of Fe-9Si measured by (Fischer et al., 2013) is fcc+hcp+B2, while Fe-8Ni-10Si (Zhang et al., 2018) is in hcp (or hcp+B2) phase. Assuming the melting curve of the Fe-8Ni-10Si (Zhang et al., 2018) is correct, the intersection point is about 250(30) GPa and 5,000 (450) K, indicating that Fe-9Si begins to melt at 250 GPa. It is larger than the data 171 (5) GPa for Fe-8Ni-10Si (Zhang et al., 2018). This difference might be caused by two reasons. The first one is that the melting curve of Fe-Si alloy (with 8.6 wt% Si) might be different with that of Fe-8Ni-10Si (Zhang et al., 2018). The second one is that the onset melting of Fe-8Ni-10Si (Zhang et al., 2018) was also not directly measured according to the sound velocity. Although the onset melting of Fe-9Si is also larger than the data of 225 GPa for Fe along Hugoniot (Nguyen & Holmes, 2004), its melting temperature is lower than the melting temperature of iron (Anzellini et al., 2013) at same pressure (Figure 5). In order to clarify the melting behavior of Fe-9Si at high pressure, especially along Hugoniot, we need more experiments, such as the sound velocity measurements near the melting region.

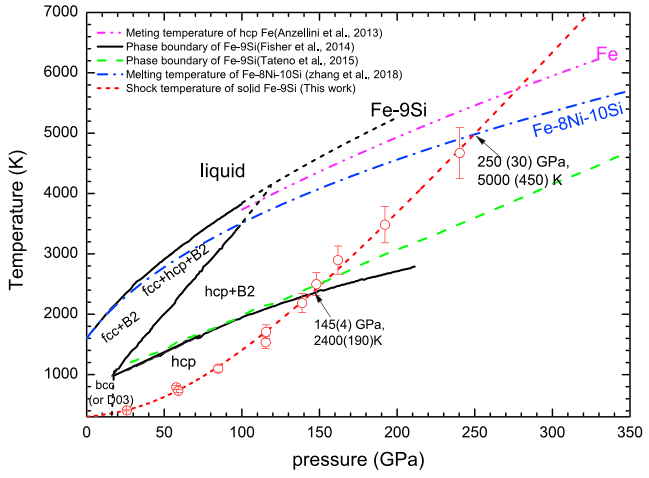

Figure 5. The shock temperature and phase diagram of Fe-9Si at high pressure. Black lines represent the phase diagram of Fe-9Si suggested by Fischer et al. (2013). The magenta dash-dot-dot line represents the melting temperature of Fe (Anzellini et al., 2013). Blue dash-dot line represents the melting curve of Fe-8Ni-10Si provided by Zhang et al. (2018). Green dash line represents the phase boundary between hcp and hcp+B2 proposed by Tateno et al. (2015). The shock temperatures of Fe-9Si are shown as red short dash line, and the open circles represent the Hugoniot data. The phase boundary between bcc to hcp is inferred according to the transformation of bcc to hcp at 16 GPa (Hirao et al., 2004; Lin et al., 2003) and the quadruple point of bcc (or D03), fcc, hcp, and B2 at about 17 GPa and 970 K. The errors of the shock temperature increase with pressure, from 2.5% at 25.8 GPa to 9% at 240.3 GPa. And this errors are mainly caused by Hugoniot parameters.

For the analysis of shock temperature, we ignored the transformation energies from bcc to hcp and from hcp to B2. Because the phase boundary of the bcc-hcp transition at 16 GPa (Hirao et al., 2004; Lin et al., 2003) is almost vertical (Figure 5), we expect the transformation energy is close to zero according to the Clapyron equation.

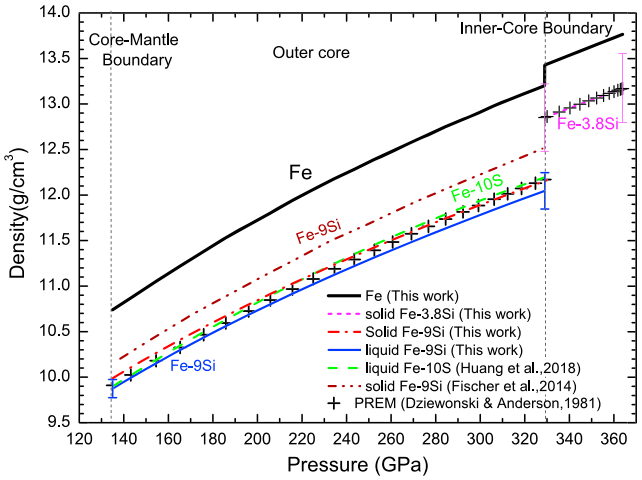

Figure 6. The density verse pressure for Fe-Si and Fe-S system in Earth's core. The data of solid and liquid Fe-9Si are shown as red dash-dot line and blue solid line. The data of Fe-9Si (Fischer et al., 2014) are drawn as a dash-dot-dot line. The data of Fe-10S (Huang et al., 2018) are shown as a green dash line. The black solid line represents the data of iron. The dot line represents the data of Fe-3.8Si under the inner core condition. The errors for density of liquid Fe-9Si are ~1 and ~2 wt% at core-mantle boundary and inner core boundary. Under the inner core condition, the errors of solid Fe-3.8 Si is about ~2.9 wt%. All the errors are propagated from the errors associated with Hugoniot parameters and temperatures in the core.

$$\Delta H = T\left(V_{hcp} - V_{bcc}\right)\frac{dP}{dT} \tag{15}$$

For the partial transition from hcp to B2 at 145±4 GPa and 2,400±190 K, it is difficult to estimate the transformation energy. However, if all the hcp Fe-9Si phase transforms to B2, the transformation energy can be estimated using equation (15). The slope of the phase boundary between hcp and B2 is constant dP/dT=0.09 GPa/K (Tateno et al., 2015). The volume difference between hcp and B2 is 0.3±0.6% (Fischer et al., 2014). Thus, the transform energy from hcp to B2 is about 0.06±0.12 MJ/Kg, which causes the temperature decreasing about 100 K above 145 GPa, which is not significant considering uncertainties associated with the experimental measurement and calculations. Table 4 lists all the thermodynamic parameters for Fe-9Si. The errors of the calculated shock temperature were estimated by assessing the uncertainties in the Grüneisen parameters and the fitted Hugoniot parameters. If the uncertainty in γ_0 =1.65 is about 10%, the corresponding uncertainty in shock temperature is about 70 K at 300 GPa, and it increases linearly with pressure. The errors of the shock temperature are mainly caused by the fitted Hugoniot parameters, which increases from 2.5% at 25.8 GPa to 9% at 240.3 GPa (Table 1 and Figure 5).

Using equations (11) and (12), the EOS for Fe-3.8Si along 300 K isotherm was also calculated. Because the content of Si is small in the Fe-3.8Si, we assumed that the thermodynamic parameters of Fe-3.8Si are similar to those of pure iron: Grüneisen parameter contributed by the lattice and electrons are γ_l=1.74$(\rho_{0\varepsilon}/\rho)^{0.78}$ (Fei et al., 2016), γ_e=2 (Anderson, 2002), and the specific heat contributed by electrons is C_{Ve}=0.091$(\rho_{0\varepsilon}/\rho)^{1.34}T$ J·Mg^{-1}·K^{-1} (Boness et al., 1986). At ambient condition, the density of hcp Fe-3.8Si is $\rho_{0\varepsilon}$=7.949 (±0.050) g/cm^3, interpolated according to the density of hcp Fe (Fei et al., 2016) and Fe-9Si under same condition. Substituting above thermodynamic parameters in to equations (11) and (12), the pressure-density data at 300 K for Fe-3.8Si were consistent with the static experimental data of Fe-9.8Ni-4Si below 210 GPa (Figure 4). Because Ni has only a marginal effect on the density of iron alloys (Asanuma et al., 2011), it is expected the densities of Fe-3.8Si and Fe-9.8Ni-4Si are similar. At the higher pressure between 210 and 270 GPa, the calculated results are slightly higher than the experimental data (Asanuma et al., 2011). Fitting the calculated data for Fe-3.8Si to third-order Birch-Murnaghan EOS yields K_0=181.9±11 GPa and K_0'=4.67±0.35.

3.3. Geophysical Implication

Using above thermodynamic parameters, we estimated the EOS for Fe-3.8Si and Fe-9Si along the temperature profile of the core $T = T_{\mathrm{ICB}}\,(\rho/\rho_{ICB})^{1.5}$.

$$P_T(V) = P_{300}(V) + \frac{1}{V}\int_{300}^{T} C_{VS}\gamma_{eff}\,dT, \tag{16}$$

$$P_T(V) = P_{300}(V) + \frac{1}{V}\int_{300}^{T_m} C_{VS}\gamma_{eff}\,dT + \frac{\gamma_{eff}}{V}\Delta S T_m + \frac{1}{V}\int_{Tm}^{T} C_{Vl}\gamma_{eff}\,dT. \tag{17}$$

T_{ICB}=5,400±300 K (Hirose et al., 2013; Zhang et al., 2018) is the temperature at inner-core boundary (ICB). ΔS=0.79±0.11 R is the melting entropy (Wallace, 1991). C_{VS} and C_{Vl} are the specific heat for solid and liquid, respectively, $C_{Vl}=C_{VS}$ -0.15RT/T_{m} (Xu & Zhang, 1986). T_{m} is the melting temperature. In the model, we assume the melting temperature of Fe-9Si close to that of Fe-8Ni-10Si (Zhang et al., 2018). Figure 6 shows the calculated density profiles for solid (red dash line) and liquid (blue solid line) Fe-9Si under outer core conditions. The effect of melting on the density, $\Delta\rho_{\mathrm{melting}}/\rho_{\mathrm{solid}}$, is estimated to be about 1.1% at 135 GPa and 0.8% at 330 GPa. This value is close to ~1.2% derived from the thermodynamic calculations (Komabayashi & Fei, 2010). Under the conditions of Earth's outer core, Fischer et al. (2014) found the densities of solid Fe-9Si is 2.4–2.7% higher than PREM profile (Dziewonski & Anderson, 1981), and they

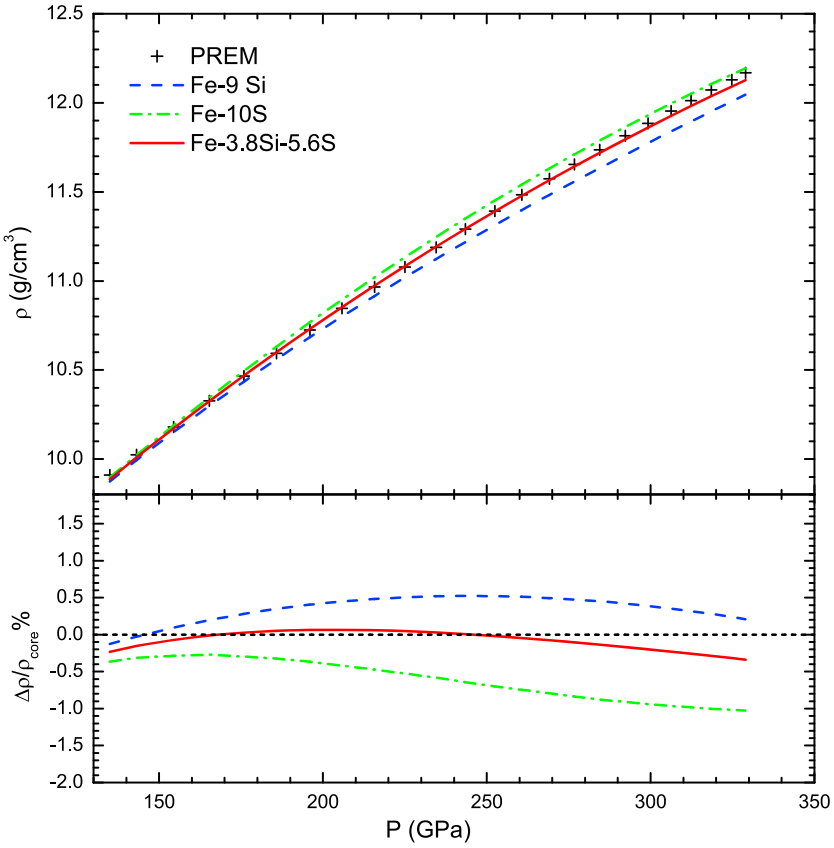

Figure 7. The density of Fe-S-Si system (a) and its difference with the PREM profile of Earth's outer core (b). Cross represents the PREM profile of Earth's outer core (Dziewonski & Anderson, 1981). The density of Fe-10S, Fe-9Si, and Fe-3.8Si-5.8S are shown as the green dash-dot line, blue dash line, and red solid line, respectively.

suggested that the content of Si is about 11.2±0.7 wt%. Our new data show that the densities of liquid Fe-9Si match with the PREM data well at the core-mantle boundary, but they are ~1.1% lower than the PREM data at the ICB. The corresponding uncertainties are ~1% and ~2.0% at core-mantle boundary and ICB, respectively.

Under the inner core conditions, the density of solid Fe-3.8Si shows a good match to the PREM profile (Figure 6). The errors for density of Fe-3.8Si are ~2.9% under inner core condition. These errors are propagated from the errors associated with Hugoniot parameters, and temperatures in the core. Using the density as the only constraint, the maximum content of Si in the liquid outer core is 8.6±2 wt%, and the solid inner core limits to 3.8±2.9 wt% Si. The sound velocity for Fe-Ni-Si alloys supports the inner core containing ~4 wt% Si (Antonangeli et al., 2010). In addition, some geochemical constraints also support this viewpoint (Wood et al., 2006). The investigation of Fe-Si phase diagrams at high pressure also implies that about 4 wt% Si in the inner core (Fischer et al., 2013). However, recent investigation on Fe-Si system indicates that Si is depleted in the inner core (Ozawa et al., 2016).

Assuming that the content of Si in the solid inner core is about 3.8 wt% and Si has an equal partitioning between the solid inner core and the liquid outer core, additional light element is required to match the observed density of the outer core. Sulfur may be the major candidate among the proposal light elements. According to the partitioning experiments of Zn between metal and silicate, Mahan et al. (2016) proposed an upper limit of 6–8 wt% S content in Earth's core. Mori et al. (2017) conducted the melting experiments on Fe-Fe_3S system up to 254 GPa, and they found 5.7±0.3 wt% S in the eutectic liquid and 3.9±0.4 wt% S in solid Fe, respectively. Huang et al. (2018) suggested that both the density and sound velocity of liquid Fe-10 wt% S match the PREM data for the liquid outer core. Of course, some scientific achievements opposed S as the main light elements of Earth's core. For example, some geochemical and cosmochemical constraints

placed the S content in the core at 2–3 wt% (e.g., Dreibus & Palme, 1996; McDonough, 2003; Suer et al., 2017). Assuming the remainder light element is sulfur, the composition of Earth's core might be Fe-S-Si. Because S and Si have the same effect on the density of iron under the outer core conditions (Figure 7), we determined that the density of Fe-3.8±2.9 Si-5.6±3.0 S best matches the observed density profile of the outer core. The proposed Fe-Si-S composition model is also in line with the geochemical constraint. Planned shockwave experiments on density and sound velocity measurements for Fe-S-Si alloys will allow us to further constrain the core composition.

4. Conclusion

In this work, we measured the Hugoniot data of Fe-9Si up to 240.3 GPa and 4,670 K with the two-stage light gas gun. The Hugoniot parameters are C_0=4.603±0.101 km/s and λ=1.505 ±0.037. The experimental data allow us to establish a reliable thermal EOS for Fe-9Si over a wide pressure-temperature range. Based on the Hugoniot data and Grüneisen EOS, we calculated isothermal EOS at 300, 1,200, 2,000, 3,000, 4,000, and 5,200 K. When using the lattice Grüneisen parameter γ_l=1.65(7.578/ρ), and electronic Grüneisen parameter γ_e=1.83, the calculated isothermal EOSs are consistent with the static compression data. Fitted the calculated pressure-density data at 300 to the third-order Birch-Murnaghan EOS yields K_0=192.1±6.3 GPa and $K_0^{'}$=4.71±0.27 with fixed density $\rho_{0\varepsilon}$ =7.578 ±0.050 g/cm^3. Combined the shock temperatures with phase diagram measured using the static compression, the shocked Fe-9Si is in bcc structure at lower pressure, and then in hcp structure at moderate pressure and temperature. At 145 GPa and 2400 K, there is detectable kink in the shock velocity and density, indicating no phase transition from hcp to B2, which is observed in the static compression. Above 250 GPa and 5000 K, the shocked Fe-9Si is in liquid state. Based on the Hugoniot parameters of Fe-9Si and Fe, the pressure-density for Fe-3.8Si along Hugoniot were determined according to additive law with the fitted Hugoniot parameters C_0=4.226±0.121 km/s and λ=1.546±0.060. And the deduced pressure-density relation at 300 K for Fe-3.8Si also agrees well with the experimental data. Under the conditions of Earth's core, the densities of liquid Fe-9Si and solid Fe-3.8Si are consistent with the PREM data of the outer core and inner core, respectively. These are the upper limits for Si in the core assuming Si is the only light element. Assuming the content of Si in the solid inner core is about 3.8 wt%, and similar amount of Si in the outer core because Si has an equal partitioning between the solid and liquid iron. Then other light element, such as sulfur, is required to match the observed density of the outer core. Based on the equations of state of Fe-9Si and Fe-10S under conditions of Earth's outer core, the density of Fe-3.8Si-5.6S were obtained and consistent with the PREM data of the outer core. Therefore, the outer core may contain 5.6±3.0 wt% S and 3.8±2.9 wt% Si. This composition not only satisfies the geophysical constraint but also satisfies the geochemical constraint.

Acknowledgments
We acknowledge the following researchers: Xiang Wang helped us during this project in the Institute of Fluid Physics; Chunhua Shen and Meijun Yang for their assistant in the Materials Research and Testing Center. This work was supported by 973 Program of China (2014CB845904), the National Science Foundation of China (41874103 and 41504070), and the Fundamental Research Funds for the Central Universities (2013-VII-25 and 2015III035). Y. F. acknowledges NSF support from the Geophysics Program (EAR-1619868). Data used in this study are available online (https://figshare.com/articles/Equation_of_State_for_Shocked_Fe-8_6_wt_Si_up_to_240_GPa_and_4670_K/8091302).

References

Allègre, C. J., Poirier, J. P., Humler, E., & Hofmann, A. W. (1995). The chemical composition of the Earth. *Earth and Planetary Science Letters*, *s5-9*(53), 351–378. https://doi.org/10.2475/ajs.s5-9.53.351

Al'tshuler, L. V., & Sharipdzhanov, I. I. (1971). Additive equation of state for silicates at high pressures. *Izvestiya Akademii Nauk SSR, Fizicheskaya Zemli*, *3*, 11–28.

Anderson, O. L. (2002). The power balance at the core-mantle boundary. *Physics of the Earth and Planetary Interiors*, *131*(1), 1–17. https://doi.org/10.1016/S0031-9201(02)00009-2

Antonangeli, D., Siebert, J., Badro, J., Farber, D. L., Fiquet, G., Morard, G., & Ryerson, F. J. (2010). Composition of the Earth's inner core from high pressure sound velocity measurements in Fe–Ni–Si alloys. *Earth and Planetary Science Letters*, *295*(1-2), 292–296. https://doi.org/10.1016/j.epsl.2010.04.018

Anzellini, S., Dewaele, A., Mezouar, M., Loubeyre, P., & Morard, G. (2013). Melting of iron at Earth's inner core boundary based on fast x-ray diffraction. *Science*, *340*(6131), 464–466. https://doi.org/10.1126/science.1233514

Asanuma, H., Ohtani, E., Sakai, T., Terasaki, H., Kamada, S., Hirao, N., & Ohishi, Y. (2011). Static compression of $Fe_{0.83}Ni_{0.09}Si_{0.08}$ alloy to 374 GPa and $Fe_{0.93}Si_{0.07}$ alloy to 252 GPa: Implications for the Earth's inner core. *Earth and Planetary Science Letters*, *310*(1-2), 113–118. https://doi.org/10.1016/j.epsl.2011.06.034

Balchan, A. S., & Cowan, G. R. (1966). Shock compression of two iron–silicon alloys to 2.7 megabars. *Journal of Geophysical Research*, *71*(14), 3577–3588. https://doi.org/10.1029/JZ071i014p03577

Birch, F. (1952). Elasticity and constitution of the Earth's interior. *Journal of Geophysical Research*, *57*(2), 227–286. https://doi.org/10.1029/JZ057i002p00227

Birch, F. (1964). Density and composition of mantle and core. *Journal of Geophysical Research*, *69*(20), 4377–4388. https://doi.org/10.1029/JZ069i020p04377

Boness, D. A., Brown, J. M., & McMahan, A. K. (1986). The electronic thermodynamics of iron under Earth core conditions. *Physics of the Earth and Planetary Interiors*, *42*(4), 227–240. https://doi.org/10.1016/0031-9201(86)90025-7

Brown, J. M., Fritz, J. N., & Hixson, R. S. (2000). Hugoniot data for iron. *Journal of Applied Physics*, *88*(9), 5496–5498. https://doi.org/10.1063/1.1319320

Brown, J. M., & McQueen, R. G. (1986). Phase transitions, Grüneisen parameter, and elasticity for shocked iron between 77 GPa and 400 GPa. *Journal of Geophysical Research*, *91*(B7), 7485–7494. https://doi.org/10.1029/JB091iB07p07485

Dreibus, G., & Palme, H. (1996). Cosmochemical constraints on the sulfur content in the Earth's core. *Geochimica et Cosmochimica Acta*, *60*(7), 1125–1130. https://doi.org/10.1016/0016-7037(96)00028-2

Dubrovinsky, L., Dubrovinskaia, N., Langenhorst, F., Dobson, D., Rubie, D., Gessmann, C., et al. (2003). Iron–silica interaction at extreme conditions and the electrically conducting layer at the base of Earth's mantle. *Nature*, *422*(6927), 58–61. https://doi.org/10.1038/nature01422

Duffy, T. S., & Ahrens, T. J. (1995). Compressional sound velocity, equation of state, and constitutive response of shock-compressed magnesium oxide. *Journal of Geophysical Research*, *100*(B1), 529–542. https://doi.org/10.1029/94JB02065

Dziewonski, A. M., & Anderson, D. L. (1981). Preliminary reference Earth model. *Physics of the Earth and Planetary Interiors*, *25*(4), 297–356. https://doi.org/10.1016/0031-9201(81)90046-7

Fei, Y., Murphy, C., Shibazaki, Y., Shahar, A., & Huang, H. (2016). Thermal equation of state of hcp-iron: Constraint on the density deficit of Earth's solid inner core. *Geophysical Research Letters*, *43*, 6837–6843. https://doi.org/10.1002/2016GL069456

Fischer, R. A., Campbell, A. J., Caracas, R., Reaman, D. M., Dera, P., & Prakapenka, V. B. (2012). Equation of state and phase diagram of Fe–16Si alloy as a candidate component of Earth's core. *Earth and Planetary Science Letters*, *357-358*, 268–276. https://doi.org/10.1016/j.epsl.2012.09.022

Fischer, R. A., Campbell, A. J., Caracas, R., Reaman, D. M., Heinz, D. L., Dera, P., & Prakapenka, V. B. (2014). Equations of state in the Fe–FeSi system at high pressures and temperatures. *Journal of Geophysical Research: Solid Earth*, *119*, 2810–2827. https://doi.org/10.1002/2013JB010898

Fischer, R. A., Campbell, A. J., Reaman, D. M., Miller, N. A., Heinz, D. L., Dera, P., & Prakapenka, V. B. (2013). Phase relations in the Fe–FeSi system at high pressures and temperatures. *Earth and Planetary Science Letters*, *373*(4), 54–64. https://doi.org/10.1016/j.epsl.2013.04.035

Hillgren, V., Gessmann, C., & Li, J. (2000). An experimental perspective on the light element in Earth's core. In R. Canup & K. Righter (Eds.), *Origin of the Earth and Moon, Lunar Planet. Inst* (pp. 245–263). Tucson, AZ: University of Arizona Press.

Hirao, N., Ohtani, E., Kondo, T., & Kikegawa, T. (2004). Equation of state of iron–silicon alloys to megabar pressure. *Physics and Chemistry of Minerals*, *31*(6), 329–336. https://doi.org/10.1007/s00269-004-0387-x

Hirose, K., Labrosse, S., & Hernlund, J. (2013). Composition and state of the core. *Annual Review of Earth and Planetary Sciences*, *41*(1), 657–691. https://doi.org/10.1146/annurev-earth-050212-124007

Huang, H., Fei, Y., Cai, L., Jing, F., Hu, X., Xie, H., et al. (2011). Evidence for an oxygen-depleted liquid outer core of the Earth. *Nature*, *479*(7374), 513–516. https://doi.org/10.1038/nature10621

Huang, H., Leng, C., Wang, Q., Yang, G., Hu, X., Wu, Y., et al. (2018). Measurements of sound velocity of liquid Fe-11.8 wt% S up to 211.4 GPa and 6,150 K. *Journal of Geophysical Research: Solid Earth*, *123*, 4730–4739. https://doi.org/10.1029/2017JB015269

Huang, H., Wu, S., Hu, X., Wang, Q., Wang, X., & Fei, Y. (2013). Shock compression of Fe-FeS mixture up to 204 GPa. *Geophysical Research Letters*, *40*, 687–691. https://doi.org/10.1002/grl.50180

Jing, F. (1986). *Introduction to experimental equation of state*. Beijing: Scientific Press.

Knittle, E., & Jeanloz, R. (1991). Earth's core–mantle boundary: Results of experiments at high pressures and temperatures. *Science*, *251*(5000), 1438–1443. https://doi.org/10.1126/science.251.5000.1438

Komabayashi, T., & Fei, Y. (2010). Internally consistent thermodynamic database for iron to the Earth's core conditions. *Journal of Geophysical Research*, *115*, B03202. https://doi.org/10.1029/2009JB006442

Li, J., & Fei, Y. (2003). Experimental constraints on core composition. In *Treatise Geochem* (Vol. 2, pp. 521–546). Oxford: Elsevier Pergamon. https://doi.org/10.1016/B0-08-043751-6/02014-4

Lin, J. F., Campbell, A. J., Heinz, D. L., & Shen, G. (2003). Static compression of iron–silicon alloys: Implications for silicon in the Earth's core. *Journal of Geophysical Research*, *108*(B1), 2045. https://doi.org/10.1029/2002JB001978

Mahan, B., Siebert, J., Pringle, E. A., & Moynier, F. (2016). Elemental partitioning and isotopic fractionation of Zn between metal and silicate and geochemical estimation of the S content of the Earth's core. *Geochimica Et Cosmochimica Acta*, *196*, 252–270. https://doi.org/10.1016/j.gca.2016.09.013

Mao, H. K., Wu, Y., Chen, L. C., & Shu, J. F. (1990). Static compression of iron to 300 GPa and $Fe_{0.8}Ni_{0.2}$ Alloy to 260 GPa: Implications for composition of the core. *Journal of Geophysical Research*, *95*(B13), 21,737–21,742. https://doi.org/10.1029/JB095iB13p21737

Marsh, S. P. (1980). *LASL shock Hugoniot data*. Berkeley: Univeisity of California Press.

McDonough, W. F. (2003). Compositional model for the Earth's core. In R. W. Carlson (Ed.), *Treatise on geochemistry* (Vol. 2, pp. 547–556). Oxford: Elsevier-Pergamon. https://doi.org/10.1016/B0-08-043751-6/02015-6

Mitchell, A. C., & Nellis, W. J. (1981). Shock compression of aluminum, copper, and tantalum. *Journal of Applied Physics*, *52*(5), 3363–3374. https://doi.org/10.1063/1.329160

Morard, G., Andrault, D., Guignot, N., Siebert, J., Garbarino, G., & Antonangeli, D. (2011). Melting of Fe–Ni–Si and Fe–Ni–S alloys at mega bar pressures: Implications for the core–mantle boundary temperature. *Physics and Chemistry of Minerals*, *38*(10), 767–776. https://doi.org/10.1007/s00269-011-0449-9

Mori, Y., Ozawa, H., Hirose, K., Sinmyo, R., Tateno, S., Morard, G., & Ohishi, Y. (2017). Melting experiments on Fe-Fe_3S system to 254 GPa. *Earth and Planetary Science Letters*, *464*, 135–141. https://doi.org/10.1016/j.epsl.2017.02.021

Nguyen, J. H., & Holmes, N. C. (2004). Melting of iron at the physical conditions of the Earth's core. *Nature*, *427*(6972), 339–342. https://doi.org/10.1038/nature02248

Ozawa, H., Hirose, K., Yonemitsu, K., & Ohishi, Y. (2016). High-pressure melting experiments on Fe–Si alloys and implications for silicon as a light element in the core. *Earth and Planetary Science Letters*, *456*, 47–54. https://doi.org/10.1016/j.epsl.2016.08.042

Poirier, J. P. (1994). Light elements in the Earth's outer core: A critical review. *Physics of the Earth and Planetary Interiors*, *85*(3-4), 319–337. https://doi.org/10.1016/0031-9201(94)90120-1

Ringwood, A. E. (1959). On the chemical evolution and densities of the planets. *Geochimica et Cosmochimica Acta*, *15*(4), 257–283. https://doi.org/10.1016/0016-7037(59)90062-6

Sakai, T., Kondo, T., Ohtani, E., Terasaki, H., Endo, N., Kuba, T., et al. (2006). Interaction between iron and post-perovskite at core-mantle boundary and core signature in plume source region. *Geophysical Research Letters*, *33*, L15317. https://doi.org/10.1029/2006GL026868

Simon, F., & Glatzel, G. (1929). Remarks on fusion pressure curve. *Zeitschrift für Anorganische und Allgemeine Chemie*, *178*(1), 309–316. https://doi.org/10.1002/zaac.19291780123

Suer, T. A., Siebert, J., Remusat, L., Menguy, N., & Fiquet, G. (2017). A sulfur-poor terrestrial core inferred from metal-silicate partitioning experiments. *Earth and Planetary Science Letters*, *469*, 84–97. https://doi.org/10.1016/j.epsl.2017.04.016

Takafuji, N., Hirose, K., Mitome, M., & Bando, Y. (2005). Solubilities of O and Si in liquid iron in equilibrium with (Mg,Fe)SiO_3 perovskite and the light elements in the core. *Geophysical Research Letters*, *32*, L06313. https://doi.org/10.1029/2005GL022773

Tateno, S., Kuwayama, Y., Hirose, K., & Ohishi, Y. (2015). The structure of Fe–Si alloy in Earth's inner core. *Earth and Planetary Science Letters*, *418*, 11–19. https://doi.org/10.1016/j.epsl.2015.02.008

Wallace, D. C. (1991). Entropy of liquid metals. *Proceedings of the Royal Society of London A*, *433*(1889), 615–630. https://doi.org/10.1098/rspa.1991.0067

Wänke, H., & Gold, T. (1981). Constitution of terrestrial planets. *Philosophical Transactions of the Royal Society of London - A*, *303*(1477), 287–302. https://doi.org/10.1098/rsta.1981.0203

Weng, J., Tan, H., Wang, X., Ma, Y., Hu, S., & Wang, X. (2006). Optical-fiber interferometer for velocity measurements with picosecond resolution. *Applied Physics Letters*, *89*(11), 111101–111101-3. https://doi.org/10.1063/1.2335948

Wood, B. J., Walter, M. J., & Wade, J. (2006). Accretion of the Earth and segregation of its core. *Nature*, *441*(7095), 825–833. https://doi.org/10.1038/nature04763

Xu, X., & Zhang, W. (1986). *Introduction to theory of equation of state*. Beijing: Scientific Press.

Zhang, J., & Guyot, F. (1999). Thermal equation of state of iron and $Fe_{0.91}Si_{0.09}$. *Physics and Chemistry of Minerals*, *26*(3), 206–211. https://doi.org/10.1007/s002690050178

Zhang, Y., Sekine, T., He, H., Yu, Y., Liu, F., & Zhang, M. (2014). Shock compression of Fe-Ni-Si system to 280 GPa: Implications for the composition of the Earth's outer core. *Geophysical Research Letters*, *41*, 4554–4559. https://doi.org/10.1002/2014GL060670

Zhang, Y., Sekine, T., He, H., Yu, Y., Liu, F., & Zhang, M. (2016). Experimental constraints on light elements in the Earth's outer core. *Scientific Reports*, *6*(1), 22473. https://doi.org/10.1038/srep22473

Zhang, Y., Sekine, T., Lin, J. F., He, H., Liu, F., Zhang, M., et al. (2018). Shock compression and melting of an Fe-Ni-Si alloy: Implications for the temperature profile of the Earth's core and the heat flux across the core-mantle boundary. *Journal of Geophysical Research: Solid Earth*, *123*, 1314–1327. https://doi.org/10.1002/2017JB014723